Theoretical investigation of mixing in warm clouds. Part 2: Homogeneous mixing

M. Pinsky(1), A. Khain(1), A. Korolev(2) and L. Magaritz-Ronen (1)

(1) Department of Atmospheric Sciences, The Hebrew University of Jerusalem, Israel

(2) Environment Canada, Cloud Physics and Severe Weather Section, Toronto, Canada

Submitted to the Atmos. Chem. Phys.

revision (April, 2016)

Communicating author: Alexander Khain, The Hebrew University of Jerusalem,

alexander.khain@mail.huji.ac.il

Abstract

Evolution of monodisperse and polydisperse droplet size distributions (DSD) during homogeneous mixing is analyzed. Time-dependent universal analytical expressions for supersaturation and liquid water content are derived. For an initial monodisperse DSD, these quantities are shown to depend on a sole non-dimensional parameter. The evolution of moments and moment-related functions in the course of homogeneous evaporation of polydisperse DSD is analyzed using a parcel model.

It is shown that the classic conceptual scheme, according to which homogeneous mixing leads to a decrease in droplet mass at constant droplet concentration, is valid only in cases of monodisperse or initially very narrow polydisperse DSD. In cases of wide polydisperse DSD, mixing and successive evaporation lead to a decrease of both mass and concentration, so the characteristic droplet sizes remain nearly constant. As this feature is typically associated with inhomogeneous mixing, we conclude that in cases of an initially wide DSD at cloud top, homogeneous mixing is nearly indistinguishable from inhomogeneous mixing.

Key words: *turbulent mixing, homogeneous mixing, mono-and polydisperse droplet size distributions*

1. Introduction

Turbulent mixing at cloud edges and cloud tops accompanied by phase transitions has been the focus of numerous studies, beginning with the pioneering works of Baker and Latham (1979), Baker et al. (1980), Blyth et al. (1980) and Baker and Latham (1982). Laboratory experiments by Latham and Reed (1977) showed that after mixing with sub-saturated air some droplets completely evaporate while others remain unchanged. This finding gave rise to the concept of two types of turbulent mixing: homogeneous and inhomogeneous. A recent description of the classical concepts of homogeneous and inhomogeneous mixing can be found in study by Korolev et al. (2016), hereafter referred to as Pt1.

Figure 1 presents a conceptual scheme of homogeneous mixing between saturated cloud volume V_1 containing droplets and sub-saturated droplet-free volume V_2 (Fig. 1a) in case of initially monodisperse droplet size distribution (DSD). This scheme is the base of further analysis. According to the concept of homogeneous mixing, the air within the volumes mixes at a rate much higher than the characteristic rate of droplet evaporation. So, the fields of temperature and humidity (and, therefore, the fields of the relative humidity and supersaturation) are rapidly homogenized throughout the entire volume, and all the droplets experience the same supersaturation (Fig. 1b). At the end of the first stage, the droplet concentration decreases due to dilution down to $N_{m0} = N_1 \frac{V_1}{V_1 + V_2}$, where N_1 is the initial droplet concentration in the cloud volume. At the second stage (Fig. 1c), droplets change supersaturation and temperature through their evaporation. There are two possible scenarios for the final equilibrium states. In the first one, illustrated in Fig. 1c, droplets continue evaporating until they saturate the environment. The size of all droplets decreases, but they evaporate only partially, so the droplet concentration N_{m0} remains unchanged. In the second scenario, when the initially droplet-free volume is very dry,

the droplets penetrated from cloud volume evaporate completely. In case of polydisperse initial DSD, both partial and complete evaporation of droplets determine the final DSD.

In contrast to homogeneous mixing, spatial homogenization during *inhomogeneous* mixing is a relatively slow process. According to the concept of extremely inhomogeneous mixing, some droplets are transported by the turbulent eddies into the dry environment and experience complete evaporation, whereas other droplets remain unchanged. As in the case of homogeneous mixing, the process of droplet evaporation continues until either the environment is saturated or all the droplets evaporate. According to the classical concept, during extremely inhomogeneous mixing the shape of DSD is conserved, however, the total droplet concentration decreases (see review by Devenish et al., 2012 and Pt 1).

The classical concepts analyze only the final equilibrium states which are based on the mass conservation consideration. Strictly speaking, the size distributions in the final states, assumed in the classical concepts, are hypothetical and cannot be reached. This is because the classic concepts do not take into account the mixing-induced DSD broadening. Detailed simulation of time evolution of DSD and other microphysical parameters is necessary not only to better determine the final states, but also to evaluate time periods during which such final states are reached. The analysis of time evolution is practically important because many DSDs measured in-situ correspond to the transient state, but not to the final equilibrium state. Besides, it is necessary to determine the evolution of initially polydisperse DSD, that may substantially differ from the evolution of monodisperse DSD.

We analyze the time evolution of the DSD during homogeneous mixing in cases of monodisperse and polydisperse initial DSDs. The analysis is based on new equations and methodology developed by Pinsky et al. (2013, 2014).

First, we need to evaluate conditions at which mixing can be considered homogeneous. The characteristic spatial scale of homogeneous mixing can be estimated by comparing the

characteristic times of two processes providing thermodynamic equilibrium inside a mixing volume. The first process is mechanical mixing (diffusion) governed by turbulence. Turbulent mixing leads to homogenization of temperature, humidity (and, thus, of supersaturation) as well as of droplet concentration within the volume $V = V_1 + V_2$. The second process is evaporation of a droplet ensemble, which leads to an increase in relative humidity and to the thermodynamical equilibrium in the mixing volume.

The process of mixing that is accompanied by droplet evaporation is characterized by two time scales. The first time scale is the characteristic mixing (homogenization) time τ_{mix} of an entrained volume with linear scale L_{mix} can be evaluated from the relationship (Monin and Yaglom, 1975)

$$\tau_{mix} = \varepsilon^{-1/3} L_{mix}^{2/3} \quad , \qquad (1)$$

where ε is the turbulent kinetic energy dissipation rate. The estimation (1) suggests that the size of the volume falls within the inertial interval of turbulence. Therefore, after the time τ_{mix}, volume with a linear scale of about L_{mix} will be mechanically homogenized and all the droplets in the volume will experience the same supersaturation.

The second time scale characterizes rate of droplet evaporation and corresponding changes of supersaturation. In this study, as well as later in Part.3, it will be shown that the characteristic evaporation time is the *phase relaxation time* τ_{pr}, that determines the rate of change of supersaturation during condensation or evaporation (Mazin, 1968; Korolev and Mazin, 2003)

$$\tau_{pr} = \left(4\pi \mathscr{D} \bar{r} N\right)^{-1}, \qquad (2)$$

where $N = N_{m0}$ is the concentration of droplets in the mixing volume, $\bar{r}$ is the mean radius of droplets and $\mathscr{D}$ is the diffusivity of water vapor. The spatial scale at which the mixing time is

equal to the phase relaxation time is called a phase relaxation scale L_{pr} (Mazin, 1968). This scale can be calculated from Eqs. (1) and (2) as

$$L_{pr} = \varepsilon^{1/2}\tau_{pr}^{3/2} \approx \varepsilon^{1/2}\left(4\pi\mathscr{D}\bar{r}N\right)^{-3/2} \quad (3)$$

The type of mixing is often characterized by the value of the Damköhler number which in regard to atmospheric mixing is defined as the ratio τ_{mix}/τ_{pr} (Baker et al., 1980; Jeffery, 2007; Lehmann et al., 2009):

$$Da = \frac{\tau_{mix}}{\tau_{pr}} = \frac{4\pi\mathscr{D}\bar{r}NL_{mix}^{2/3}}{\varepsilon^{1/3}} \quad (4)$$

The case $Da \ll 1$ corresponds to homogeneous mixing, when mechanical homogenization occurs much faster than does droplet evaporation. The case $Da \gg 1$ corresponds to extremely inhomogeneous mixing. It is reasonable to consider the value $Da = 1$ as a boundary separating the two types of mixing. This condition is equivalent to the condition

$$L_{mix} = L_{pr} \approx \varepsilon^{1/2}\left(4\pi\mathscr{D}\bar{r}N\right)^{-3/2} \quad (5)$$

Expression (5) determines the maximum spatial scale at which mixing can be considered as homogeneous. The evaluation of the spatial scales at conditions typical of different cloud types is presented in **Table 1**. One can see that the characteristic volume size at which mixing can be considered homogeneous ranges from 0.2 m to 0.6 m. At larger scales, supersaturation within the mixing volume is non-uniform and droplets in the volume experience different values of relative humidity. In this case, the mixing should be considered inhomogeneous.

The further paper structure is the following. In Section 2 we calculate the thermodynamic characteristics of the resulting volume at the end of the first stage of mixing (see Fig. 1b).

143 Section 3 presents an analytic solution of homogeneous droplet evaporation in the monodisperse
144 DSD case. In Section 4 effects of polydispersivity on the DSD evolution are described. The
145 problem of turbulent mixing representation in numerical cloud models is discussed in Section 5.
146 The main results of the study are presented in Conclusion Section 6.
147

148 **2. Thermodynamic characteristics of the mixing volume at the end of the first stage**

149 At the first stage (see the scheme in Fig.1) homogeneous mixing is considered as an isobaric
150 process that is not accompanied by phase transitions (Korolev and Isaac, 2000). Let us consider
151 mixing between a cloud volume with mass m_1, supersaturation $S_1 = 0$ and temperature T_1 and a
152 droplet-free volume with mass m_2, supersaturation $S_2 < 0$ and temperature T_2. The cloud
153 volume also contains droplets with concentration N_1 and liquid water mixing ratio q_1 (Fig. 1).
154 For the sake of simplicity, we assume that the mass of both volumes is equal to one. Let us
155 further assume that μ is the mass fraction of the cloud air that mixes with the mass fraction
156 $(1-\mu)$ of the droplet-free air. In this case, the air mass in the mixing volume will be equal to
157 $m_1\mu + (1-\mu)m_2 = 1$. Isobaric mixing leads to an approximate linear dependence of droplet
158 concentration N_{m0} on μ.

159 After an instantaneous homogenization of the two volumes, the intermediate temperature
160 T_{m0}, droplet concentration N_{m0} and liquid mixing ratio q_{m0} are (see Pt.1):

161 $$N_{m0} = N_1\mu; \quad q_{m0} = q_1\mu; \quad T_0 = T_1\mu + T_2(1-\mu) \qquad (6a)$$

162 If the temperature difference $|T_1 - T_2|$ does not exceed a few degrees, the intermediate
163 supersaturation S_{m0} can be approximated by a linear dependence on μ

164 $$S_{m0} = S_2(1-\mu) \qquad (6b)$$

Figure 2 shows, that in case $|T_1 - T_2| < 2^{o}C$, the deviations of supersaturation from the linear dependence (6b) are small enough and can be neglected. In cases when the temperature of the dry volume substantially differs from the temperature of the cloud volume, the dependence of the resulting supersaturation on parameter μ becomes non-linear (Fig. 2). At temperature differences of 5-10 ^{o}C, the deviation from the analytical solution (6) increases, which requires using more precise formulas for supersaturation (see Pt. 1). Values of N_{m0}, q_{m0}, T_{m0} and S_{m0} determine the initial conditions for the second stage of homogeneous mixing. This is actually homogeneous evaporation of droplets, which leads to a thermodynamic equilibrium between water vapor and liquid water.

3. Analysis of homogeneous droplet evaporation in the monodisperse DSD case

3.1. Basic assumptions and equations

The second stage of mixing consists in homogeneous evaporation of droplets. The evolution of DSD during the second stage is considered here under the following assumptions: a) the processes inside the mixing volume are adiabatic, b) the droplet size distribution is monodisperse, c) the vertical velocity of the volume $u_z = 0$ and d) the sedimentation of droplets is neglected and their concentration remains constant.

The liquid water mixing ratio can be expressed as

$$q(t) = \frac{4\pi\rho_w}{3\rho_a} N r^3(t) \qquad (7)$$

where $r(t)$ is the radius of droplets and N is the droplet number concentration. Closed equations describing condensation/evaporation in a moving adiabatic air volume were obtained

188 by Pinsky et al. (2013). In an unmoving adiabatic volume, evaporation is described by the
189 equation for supersaturation (e.g., Korolev and Mazin, 2003)

190 $$\frac{1}{S+1}\frac{dS}{dt} = -A_2\frac{dq}{dt} \qquad (8)$$

191 and droplet evaporation is described by the simplified equation (Pruppacher and Klett, 2007)

192 $$r\frac{dr}{dt} = \frac{S}{F}, \qquad (9)$$

193 where S is the supersaturation over a flat water surface. For cloud droplets Eq. (9) is valid with
194 high accuracy. We do take into account formation of haze particles resulting from droplet
195 evaporation. This allows us to neglect the curvature term and chemical term in the evaporation
196 equation. Coefficients A_2 and F in Eqs. (8, 9) are slightly dependent on the temperature and the
197 pressure

198 $$A_2 = \frac{1}{q_v} + \frac{L^2}{c_p R_v T^2} \qquad (10)$$

199 $$F = \frac{\rho_w L^2}{k_a R_v T^2} + \frac{\rho_w R_v T}{e_S(T)\mathscr{D}} \qquad (11)$$

200 We assume that coefficients A_2 and F do not change in the course of droplet evaporation.
201 The physical meaning and units of other variables are given in **Appendix A.**
202

203 **3.2. Time evolution of supersaturation and of liquid water content**

204 The closed differential equations for the liquid water mixing ratio q and supersaturation S
205 to be used in the analysis are derived in **Appendix B.**

206 $$\frac{dq}{dt} = BN_{m0}^{2/3}\left[(S_{m0}+1)\exp\{-A_2(q-q_{m0})\}-1\right]q^{1/3} \qquad (12)$$

207 $$\frac{1}{S+1}\frac{dS}{dt} = -A_2 BN_{m0}^{2/3} S\left(q_{m0} - \frac{1}{A_2}\ln\frac{S+1}{S_{m0}+1}\right)^{1/3} \qquad (13)$$

where

$$B = \frac{3}{F}\left(\frac{4\pi\rho_w}{3\rho_a}\right)^{2/3} = const \qquad (14)$$

The solutions of these equations depend on the values of N_{m0}, q_{m0}, T_{m0}, and S_{m0}, obtained after the first stage of mixing. Eqs. (12) and (13) are rigidly connected by the following equation directly following from Eq. (8):

$$\ln[S(t)+1] = -A_2 q(t) + C \qquad (15)$$

where $C = \ln[S_{m0}+1] + A_2 q_{m0}$ is determined by the initial conditions at $t = 0$.

Since in this study we assume $S(t) \le 0$, it is convenient to use the relative humidity RH and the saturation deficit SD to characterize the thermodynamic state of the mixing volume. Both quantities are easily related to $S(t)$: $SD(t) = -S(t)$, $RH(t) = 1 + S(t)$. **Figure 3** demonstrates dependencies $S(t)$ and $q(t)$, calculated at an initial relative humidity RH_{m0} that varies from 72% to 91.6%, and an initial LWC of 0.6 gm^{-3}. RH_{m0} corresponds to the relative humidity in dry volume RH_2, that ranges from 43% to 83% at $\mu = 0.5$. The results of solving Eqs. (14-15) were compared with those obtained using a parcel model (Korolev, 1995) in which evaporation is described using equations with temperature-dependent parameters, and were found to be in excellent agreement. This agreement can be attributed to the fact that temperature changes that occurred in the course of the mixing are relatively small, validating the assumption about the constancy of A_2 and F.

As seen from Fig. 3, the final equilibrium state may be reached within several seconds. Fig. 3 shows the possibility of the two final states mentioned above: a) complete droplet evaporation

reached at different time instances depending on the initial value of S_{m0}, and b) partial droplet evaporation at $RH_{m0} > 82\%$. In the latter case, the final supersaturation is equal to zero.

3.3. Universal dependencies of supersaturation and of LWC on time

In order to simplify the further analysis we introduce the following non-dimensional parameters: normalized liquid water mixing ratio $\tilde{q} = \frac{q}{q_{m0}}$ which is equal to normalized liquid water content, normalized supersaturation $\tilde{S} = \frac{S}{A_2 q_{m0}}$, and non-dimensional time $t = t/\tau_{m0}$, where $\tau_{m0} = \left(BA_2 N_{m0}^{2/3} q_{m0}^{1/3}\right)^{-1}$ is the time scale. Then the set of non-dimensional equations describing changes of supersaturation and liquid mixing ratio can be written as (see Appendix B for detail)

$$\tilde{S}(\tilde{t}) = -\tilde{q}(\tilde{t}) + \gamma \tag{16}$$

$$\frac{d\tilde{q}}{d\tilde{t}} = \tilde{q}^{1/3}\left(\gamma - \tilde{q}\right) \tag{17}$$

$$\frac{d\tilde{S}}{d\tilde{t}} = -(\gamma - \tilde{S})^{1/3}\tilde{S}, \tag{18}$$

where

$$\gamma = 1 + \frac{S_{m0}}{A_2 q_{m0}} = 1 + \frac{1-\mu}{\mu}\frac{S_2}{A_2 q_1} \tag{19}$$

is dimensionless parameter which depends on the initial supersaturation S_{m0} and the initial liquid water mixing ratio q_{m0}. The value of this parameter can be either positive or negative. Eqs. (16-18) are strictly valid if $|S_{m0}| << 1$, i.e. when the value of supersaturation S is negligible in comparison with unity in the factor $(S+1)^{-1}$ on the left-hand side of Eq. (8). However, a detailed comparison of solutions of Eqs. (16-18) with those obtained using a numerical model showed

that Eqs. (16-18) provide accurate solution at RH_{m0} as low as 30-40%. Eq. (17) should be solved with the initial condition $\tilde{q}(0)=1$, and Eq. (18) should be solved with the initial condition $\tilde{S}(0)=\frac{S_{m0}}{A_2 q_{m0}}<0$. Therefore, solutions of both equations depend on the sole parameter γ. Eqs. (17) and (18) are rigidly connected by balance equation Eq. (16).

Defining $x(\tilde{t})=\left(\tilde{q}(\tilde{t})\right)^{1/3}$ and $\chi=|\gamma|^{1/3}\mathrm{sgn}(\gamma)$, the solution of Eq. (17) with the initial condition $x(0)=1$ is

$$2\chi\tilde{t}=\ln\left[\frac{(1-\chi)^2}{(x-\chi)^2}\frac{x^2+\chi x+\chi^2}{1+\chi+\chi^2}\right]+2\sqrt{3}\left[\mathrm{atan}\frac{2\sqrt{3}\chi(1-x)}{3\chi^2+(2+\chi)(2x+\chi)}\right] \qquad (20)$$

The solution for the normalized supersaturation can be obtained from Eq. (20) and the balance equation (16)

$$\tilde{S}(\tilde{t})=-\tilde{q}(\tilde{t})+\gamma=-x^3(\tilde{t})+\chi^3 \qquad (21)$$

Figure 4 demonstrates time dependencies $\tilde{S}(\tilde{t})$ and $\tilde{q}(\tilde{t})$ calculated at different γ at $S_{m0}>-10\%$ (i.e. $RH_{m0}>90\%$). As seen from Fig. 4. the analytical solution is quite close to the numerical one. The deviation increases with an increase in parameter γ. At $\gamma=-0.5$, the error in the final *RH* is about 15%. The initial RH_{m0} in this case is about 90 %. RH_{m0} is the relative humidity in the mixing volume V after the first stage of mixing. As mentioned above, RH_{m0} may be substantially higher than RH_2 in the initially droplet-free volume. *In-situ* measurements (Gerber et al., 2008) and remote measurements of aerosol humidification (Knight and Miller, 1998; Bar-Or et al., 2012) indicate the existence of zones of high *RH* along cloud edges. These observations and results of numerical simulations indicate that the analytical solution (20-21) is a universal one and applicable at any RH values in cloud surrounding.

The amplitude of the deviation of the analytical solution for supersaturation from the modeled result decreases with the decrease of γ. The cause of the deviation is neglecting term $(S+1)$ on the left-hand side of Eq. (8).

There are two types of solutions determined by parameter χ (or parameter γ), separated by value $\chi = 0$ (Figs. 3 and 4). Condition $\chi = 0$ corresponds to $\mu = \mu_{cr}$ (see Pt 1) and indicates complete evaporation of all the droplets and the relative humidity increasing up to 100 %. Condition $\chi > 0$ corresponds to solutions $\tilde{q}(\tilde{t})$ with asymptotic behavior at $\tilde{t} \to \infty$: $\tilde{q} \to \gamma$ and $\tilde{S} \to 0$, which means that droplets do not completely evaporate. Condition $\chi < 0$ means that all the droplets completely evaporate.

At $\chi = 0$, the analytical solution is:

$$x = \frac{3}{\tilde{t}+3}; \quad \tilde{q}(\tilde{t}) = \left(\frac{3}{\tilde{t}+3}\right)^3; \quad \tilde{S}(\tilde{t}) = -\left(\frac{3}{\tilde{t}+3}\right)^3 \tag{22}$$

Both LWC and supersaturation tend to zero at $\tilde{t} \to \infty$.

At $\chi < 0$, the duration of the evaporation is limited in time (Figs. 3, 4). Normalized evaporation time t_e depends on parameter χ only. This dependence can be obtained from Eq. (20) at $x = 0$:

$$t_e = \frac{1}{2\chi} \ln \frac{(1-\chi)^2}{1+\chi+\chi^2} + \frac{\sqrt{3}}{\chi} \operatorname{atan} \frac{\sqrt{3}}{2\chi+1} \tag{23}$$

Here the time is counted in the relaxation time scales. This fact indicates that the phase relaxation time is the time scale that should be used in the analysis of mixing. The choice of a time scale will be discussed elaborated in greater detail below.

289 At $\chi > -1/2$, one have to use the values $\operatorname{atan}\left(\frac{\sqrt{3}}{2\chi+1}\right)-\pi$ in Eq. (23) instead of $\operatorname{atan}\frac{\sqrt{3}}{2\chi+1}$.

290 t_e is the time needed for supersaturation to reach its maximal value (Figs. 3a, 4a). This value is
291 calculated from Eqs. (16) and (6)

292 $$\tilde{S}_{\max} = \gamma = \chi^3 = 1 + \frac{S_{m0}}{A_2 q_{m0}} \approx 1 + \frac{S_2}{A_2 q_1}\frac{1-\mu}{\mu} = 1 + R\frac{1-\mu}{\mu} \qquad (24)$$

293 where $R = \frac{S_2}{A_2 q_1}$ is a dimensionless parameter describing the ratio of S_2 in the initially dry air
294 and the reserve of liquid water available for evaporation. (This parameter can be determined
295 more precisely using Eq. (2) or Eq. (4) given in Pt. 1).

296 The dependence $t_e(\chi)$ is shown in **Figure 5. O**ne can see that at large sub-saturation values
297 ($\chi < -0.4$) all the droplets evaporate within the span of a few relaxation times, and the analytical
298 results agree well with the model (benchmark) results. At a high initial *RH*, droplet evaporation
299 increases the humidity to nearly the saturation value, at which evaporation becomes extremely
300 slow. In this case, simplified analytical formulas overestimate the evaporation time.

301 At $\chi > 0$**,** droplets partially evaporate, q reaches the minimal value and the thermodynamic
302 equilibrium is reached when $S \to 0$. Minimal normalized equilibrium LWC can be found from
303 Eqs. (21) and (6)

304 $$\tilde{q}_{\min} = \gamma = \chi^3 = 1 + R\frac{1-\mu}{\mu} \qquad (25)$$

305 Eq. (25) is similar to Eqs. (4-5) (see Pt.1.).

306 Dependences of $\tilde{S}_{\max}$ and $\tilde{q}_{\min}$ on cloud air fraction, calculated at different initial conditions
307 using Eqs. (24) and (25) are shown in **Figure 6**. The diagram in Fig. 6b is actually a kind of
308 widely used mixing diagram for homogeneous mixing, and Eq. (25) is an universal analytic
309 equation for calculation of this diagram depending on the non-dimensional parameter R. Panel

(a) shows that the higher the cloud fraction of air parcels involved in mixing, the lower the saturation deficit, i.e. the higher the final *RH* is. At small R, saturation is reached at a low μ. Similar diagrams in physical units are shown in Pt.1 in Figs. 4a,g.

The equations presented above allow to predict the results of homogeneous mixing both for partial and complete evaporation of droplets (**Table 2)**. One can see that at low temperatures, the environment air volume becomes cloudy at relatively low values of liquid water content in the cloud volume even if *RH* of the environment volume is as low as 50%. The reason is that the saturation ratio at low temperatures is low and only a small amount of liquid should be evaporated to make the initially dry volume saturated.

The diagram in Fig.6b allows to calculate the final liquid water content remaining in the entire volume after saturation reaches 100%. This diagram also shows that for each value of μ there is a certain value of R at which full evaporation takes place. The remaining $\tilde{q}_{\min}$ increases with decreasing μ and increasing R, as shown by the arrow.

The natural time scale of the evaporation and, therefore, homogeneous mixing was determined as $\tau_{m0} = \left(BA_2 N_{m0}^{2/3} q_{m0}^{1/3}\right)^{-1}$. This value is inversely proportional to $N_{m0} r_{m0}$ and actually coincides with the initial phase relaxation time τ_{pr}. The equality of the characteristic time scales of variations in supersaturation and in liquid water content directly follows from the equation (15). Indeed, in case of $|S| << 1$ the equation can be rewritten as $S(t) = -A_2 q(t) + C$ thus establishing a linear relationship between the supersaturation and the liquid water mixing ratio.

It should be emphasized that τ_{m0} is not the time of total droplet evaporation or the time of reaching saturation (when evaporation is over). The time of complete evaporation of all droplets can be substantially longer than phase relaxation time τ_{m0}.

4. Analysis of homogeneous droplet evaporation in case of a polydisperse DSD

334 **4.1. DSD evolution in the course of droplet evaporation**

335 To analyse polydisperse DSD evolution during droplet evaporation at the second stage of
336 homogeneous mixing, we use the same equations for diffusional growth (9) and supersaturation
337 (8) as those used in case of a monodisperse DSD. The solution of Eq. (9) can be written in the
338 form

339 $$r^2(t) = r_0^2 - Q(t) \tag{26}$$

340 where the non-negative function $Q(t) \geq 0$ is proportional to the supersaturation integral

341 $$Q(t) = -\frac{2}{F}\int_0^t S(t')dt' \geq 0 \tag{27}$$

342 This function characterizes a decrease in the square of droplet radii. At $t = 0$, $Q(0) = 0$. Let
343 $f_0(r_0)$ be an initial DSD immediately following the first stage of homogeneous mixing. This
344 distribution obeys the normalization condition

345 $$N_{m0} = \int_0^\infty f_0(r_0)dr_0 \tag{28}$$

346 where N_{m0} is the initial droplet number concentration after the first stage of mixing. Using the
347 inverse transformation $r_0 = \sqrt{r^2 + Q(t)}$ alongside with condition $r \geq 0$ and the relation between
348 the distribution functions $f(r,t) = f_0(r_0)\frac{dr_0}{dr}$ we get

349 $$f(r,t) = \begin{cases} \dfrac{r}{\sqrt{r^2 + Q(t)}} f_0\left(\sqrt{r^2 + Q(t)}\right), & r \geq 0 \\ 0, & r < 0 \end{cases} \tag{29}$$

350 Eq. (29) shows that the time changes in DSD and in its moments depend both on the initial DSD
351 at $t = 0$, $f_0(r_0)$ and on the time-dependent function $Q(t) \geq 0$.

352 To illustrate the DSD evolution using Eq. (29), we assume that the initial distribution
353 immediately following the first stage of mixing can be represented by a Gamma distribution:

$$f_0(r_0) = \frac{N_{m0}}{\Gamma(\alpha)\beta}\left(\frac{r_0}{\beta}\right)^{\alpha-1}\exp\left(-\frac{r_0}{\beta}\right) \quad (30)$$

where N_{m0} is an intercept parameter, α is a shape parameter and β is a slope parameter of distribution. Different sets of parameters allow approximations of both narrow and wide DSD. The parameters of the initial Gamma distribution used in this study are presented in **Table 3** and are chosen so that the modal radii of DSD and the LWC would be the same for both distributions.

Combining Eqs. (29) and (30) yields an equation for DSD evolution as a function of $Q(t)$

$$f(r,t) = \begin{cases} \dfrac{N_{m0}}{\Gamma(\alpha)\beta^{\alpha}}(r^2+Q)^{\frac{\alpha}{2}-1} r \exp\left(-\dfrac{\sqrt{r^2+Q}}{\beta}\right), & r \geq 0 \\ 0, & r < 0 \end{cases} \quad (31)$$

This DSD (31) depends on four parameters, wherein parameter $Q(t)$ increases with time according to Eq. (27). Examples of evolutions of an initially narrow DSD and an initially wide DSD are shown in **Figure 7**. All the calculations were performed using a parcel model (Korolev, 1995).

There is a significant difference between evolution of DSDs in cases of monodisperse and polydisperse DSDs. At a monodisperse DSD, droplet concentration remains unchanged until the final stage of evaporation when droplets become small and then all evaporate rapidly. At a polydisperse DSD the droplet concentration decreases simultaneously with the decrease in LWC. Evaporation of a the narrow size distribution is consistent with the concept of homogeneous mixing (Fig. 7a). However homogeneous evaporation of droplets with a wide DSD may be mistakenly taken for inhomogeneous mixing.

4.2. Evolution of DSD moments and related functions

Eq. (29) also allows evaluation of droplet concentration, DSD moments and related functions. Droplet concentration corresponds to the zero moment of DSD and can be expressed as

$$N(t)=\int_0^\infty f(r,t)dr=\int_0^\infty \frac{r}{\sqrt{r^2+Q(t)}}\,f_0\left(\sqrt{r^2+Q(t)}\right)dr=\int_{\sqrt{Q(t)}}^\infty f_0(r_0)dr_0 \qquad (32)$$

Since function $Q(t)$ monotonically increases with the time, the right-hand integral in Eq. (32) decreases, indicating a decrease in droplet concentration with time. If the initial distribution of droplets is described by a Gamma distribution, the decrease of droplet concentration with the time is evaluated using Eqs. (30) and (32) as

$$N(t)=\int_{\sqrt{Q(t)}}^\infty f_0(r_0,t)dr_0=\int_{\sqrt{Q(t)}}^\infty \frac{N_{m0}}{\Gamma(\alpha)\beta}\left(\frac{r_0}{\beta}\right)^{\alpha-1}\exp\left(-\frac{r_0}{\beta}\right)dr_0=$$

$$\frac{N_{m0}}{\Gamma(\alpha)}\int_{\frac{\sqrt{Q(t)}}{\beta}}^\infty x^{\alpha-1}\exp(-x)dx=N_{m0}\frac{\Gamma(\alpha,\eta)}{\Gamma(\alpha)}. \qquad (33)$$

where

$$\eta(t)=\frac{\sqrt{Q(t)}}{\beta} \qquad (34)$$

is a non-dimensional function of time and $\Gamma(\alpha,\eta(t))$ is an upper incomplete Gamma function (Korn and Korn, 2000). It follows from Eqs. (32) and (33) that $N(t)\le N_0$. The dependencies of the normalized droplet concentration $\frac{N(t)}{N_{m0}}$ on time for an initially narrow DSD and an initially wide DSD are shown in **Figure 8**.

Fig. 8 shows that in case of an initially narrow DSD, droplet concentration does not change during the first 20 s when $RH_{m0}=91.6$ % because the DSD does not shift strongly enough toward smaller droplet radii. At lower initial supersaturations, droplet concentration decreases

with time. This decrease may take place rapidly and may last several seconds only. The red line separates two different evaporation scenarios. The curves above the red line correspond to partial evaporation and reaching the saturation state, whereas the curves below the red line correspond to complete evaporation of droplets and the environment remains subsaturated.

At an initially wide DSD, droplet concentration decreases at any initial subsaturation value because the DSD contains small droplets that start evaporating regardless the subsaturation value. In the particular example shown in Fig. 8, the droplet relaxation time is shorter in case of a wide DSD, so droplet concentration decreases slower than at a narrow DSD. Droplet concentration decreases substantially during a few tens of seconds, but does not reach zero due to a significant concentration of large droplets in the wide DSD. The equilibrium state is not reached within 20 s.

Fig. 8 also demonstrates an excellent agreement between the results of analytical calculations performed using Eq. (33) and results obtained using the parcel model.

A normalized moment of the *k-th* order is evaluated as

$$\overline{r^k(t)} = \frac{1}{N(t)}\int_0^\infty r^k f(r,t)dr = \frac{1}{N(t)}\int_0^\infty \frac{r^{k+1}}{\sqrt{r^2+Q(t)}} f_0\left(\sqrt{r^2+Q(t)}\right)dr =$$

$$\frac{1}{N(t)}\int_{\sqrt{Q(t)}}^\infty \left(r_0^2 - Q(t)\right)^{k/2} f_0(r_0)dr_0$$

$$\overline{r^k(t)} = \frac{\int_{\sqrt{Q(t)}}^\infty \left(r_0^2 - Q(t)\right)^{k/2} f_0(r_0)dr_0}{\int_{\sqrt{Q(t)}}^\infty f_0(r_0)dr_0} \qquad (35)$$

In case when the initial distribution is given by the Gamma distribution (30), Eq. (35) leads to the following equation

$$\overline{r^k}(t) = \frac{\beta^k}{\Gamma\left(\alpha,\eta(t)\right)}\int_{\eta(t)}^\infty \left(x^2-\eta^2(t)\right)^{k/2}\left(x\right)^{\alpha-1}\exp\left(-x\right)dx \qquad (36)$$

415 The even moments can be represented using incomplete the Gamma functions.

416 **Figures 9 and 10** show the time dependencies of quantities typically used for characterizing

417 the DSD shape, namely the mean radius $\overline{r}(t)$ (panel (a)), the effective radius $r_{eff}(t) = \frac{\overline{r^3}(t)}{\overline{r^2}(t)}$

418 (panel (b)), the RMS width of DSD $\sigma(t) = \sqrt{\overline{r^2}(t) - \overline{r}^2(t)}$ (panel (c)) and the dispersion

419 coefficient $\delta(t) = \frac{\sigma(t)}{\overline{r}(t)}$ (panel (d)). The dependencies corresponding to an initially narrow DSD

420 are shown in Fig. 9 and those corresponding to an initially wide DSD are shown in Fig. 10.

421 At an initially narrow DSD, the mean radius and the effective radius decrease with time in

422 agreement with the concept of homogeneous mixing. Formation of plateaus in the mean radii, in

423 the effective radii and in droplet dispersion over long time periods is caused by the existence of

424 droplets in the tail of DSD distributions. While the concentration of such droplets is negligibly

425 small, their evaporation takes a significant amount of time.

426 At an initially wide DSD (Fig.7b), complete evaporation of the smallest droplets starts at the

427 very beginning of the second stage of mixing. This evaporation leads to an increase in the

428 effective radius and in the mean radius that changes non-monotonically. An increase in the

429 value of the effective radius contradicts the concept of homogeneous mixing, according to which

430 both the mean radii and the effective radii decrease in the course of mixing. This increase is

431 explained by the fact that subsaturation at an initially wide DSD leads to a significant rapid

432 decrease in the concentration of small droplets, while the changes in LWC whose value is

433 determined by larger droplets, do not occur that quickly.

434 The opposite behaviors of the effective radii (as well as of the other characteristic droplet

435 sizes) at a narrow DSD vs. a wide DSD, illustrated in Figs. 9 and 10, suggest the existence of a

436 large number of DSDs with initial shapes at which the evaporation of droplets leads to a decrease

437 in droplet concentration, but does not change significantly the effective radius. So the constancy

438 of the effective radius at varying droplet concentrations does not allow to distinguish the mixing
439 type with full confidence. Even at a narrow DSD, the decrease in the value of the effective radius
440 does not exceed 20% at the an initial saturation deficit of 8.4 %.

441 In any case the evolution of DSD and of their parameters is determined by the competition
442 between two effects. First, this is the effect of partial droplet evaporation which shifts the DSD
443 toward smaller sizes and leads to a decrease in the mean radii and in the effective radii, as well
444 as widens the DSD. Second, this is the effect of complete evaporation of the smallest droplets,
445 which increases both the mean radii and the effective radii. The relative contribution of these two
446 effects depends on the initial DSD width and the value of the mean radius. The best indicators of
447 these two effects are the DSD width, σ and the DSD dispersion $\frac{\sigma}{\overline{r}}$.

448 At an initially narrow DSD and an initially low *RH*, partial evaporation initially dominates
449 and the DSD width increases due to the appearance of smaller droplets (Fig. 9c). Afterwards,
450 when complete droplet evaporation becomes the dominant factor, the DSD shifts significantly to
451 small sizes and the DSD width decreases. At an initially large *RH*, complete droplet evaporation
452 is not efficient, and the DSD gets continuously wider. Since the mean radius decreases, the DSD
453 dispersion tends to constant values at any initial *RH*. However, the largest DSD dispersion takes
454 place at an initially low *RH*, when evaporation substantially decreases the mean droplet radius.
455 As seen in Figs. 9d and 10d, the initial DSD dispersion at a narrow DSD is 0.1, while the initial
456 dispersion at a wide DSD is 0.5.

457 Figs. 10c and 10d show that at an initially wide DSD, homogeneous evaporation leads to an
458 increase in both DSD width and DSD dispersion. The increase in the DSD width indicates that
459 formation of the smallest droplets by partial evaporation is the main mechanism of the DSD
460 shape evolution. The DSD dispersion increases with time and rapidly reaches quasi-stationary
461 values of about 0.56 that are typical of real clouds.

462

463 **4.3. Evolution of LWC and of supersaturation**

464 Using Eq. (35), the time dependence of the liquid water mixing ratio is represented as

465 $$q(t)=\frac{4\pi\rho_w}{3\rho_a}N(t)\overline{r^3(t)}=\frac{4\pi\rho_w}{3\rho_a}\int\limits_{\sqrt{Q(t)}}^{\infty}\left(r_0^2-Q(t)\right)^{3/2}f_0(r_0)dr_0 \qquad (37)$$

466 If the initial DSD is approximated by a Gamma distribution, $q(t)$ can be written as

467 $$q(t)=\frac{4\pi\rho_w}{3\rho_a}\int\limits_{\sqrt{Q(t)}}^{\infty}\left(r_0^2-Q(t)\right)^{3/2}\frac{N_{m0}}{\Gamma(\alpha)\beta}\left(\frac{r_0}{\beta}\right)^{\alpha-1}\exp\left(-\frac{r_0}{\beta}\right)dr_0= \frac{4\pi\rho_w}{3\rho_a}\frac{N_{m0}\beta^3}{\Gamma(\alpha)}\int\limits_{\eta(t)}^{\infty}\left(x^2-\eta^2(t)\right)^{3/2}(x)^{\alpha-1}\exp(-x)dx \qquad (38)$$

468 Since at $t=0$, $\eta=0$ and the initial liquid water mixing ratio is equal to

469 $q_{m0}=\frac{4\pi\rho_w}{3\rho_a}N_{m0}\beta^3\frac{\Gamma(\alpha+3)}{\Gamma(\alpha)}$, hence the normalized liquid water mixing ratio is calculated as

470 $$\frac{q(t)}{q_{m0}}=\frac{1}{\Gamma(\alpha+3)}\int\limits_{\eta(t)}^{\infty}\left(x^2-\eta^2(t)\right)^{3/2}(x)^{\alpha-1}\exp(-x)dx \qquad (39)$$

471

472 **Figure 11** shows the time dependencies of LWC for different initial RH_{m0} in the resulting
473 volume (Fig.11a: an initially narrow DSD; Fig.11b: an initially wide DSD). One can see that at
474 an initially narrow DSD the LWC rapidly decreases, either to zero (full evaporation) or, as in the
475 monodisperse case, to an equilibrium value during a time period of the phase relaxation time (see
476 Section 3 for comparison). At an initially wide DSD, the LWC decreases slowly and
477 monotonically. In general, at an initially narrow DSDs the time dependencies, $q_w(t)$ are quite
478 close to those for monodisperse DSD (Fig. 3b). The higher the initial *RH*, the smaller the change
479 in the LWC is.

480 To calculate the time dependencies of supersaturation, one can use the full equation (8) or
481 Eq. (15) written in the form:

$$S(t) = (S_{m0} + 1)\exp\left\{-A_2\left[q(t) - q_{m0}\right]\right\} - 1 \qquad (40)$$

In Eq. (40), S_{m0} and q_{m0} are the initial supersaturation and the liquid water mixing ratio, respectively, at $t = 0$. The corresponding time dependencies are shown in **Figure 12.** The analytical results of Eq. (40) are compared with the exact numerical solution obtained by a parcel model, showing a good agreement. The behavior of supersaturation at a initially narrow DSD is similar to that of a monodisperse DSD (Fig. 3a). As in Fig. 3a, the equilibrium non-zero values of subsaturation correspond to complete droplet evaporation. At initially wide DSD, the saturation deficit monotonically decreases as a consequence of the monotonic decrease in the LWC.

Figure 13 shows the dependencies of normalized LWC on normalized droplets concentrations calculated at different values of the initial relative humidity RH_{m0} in the mixing volume ((a): the initially narrow DSD and (b) the initially wide DSD). Each point on the curves corresponds to a certain time. Since the dependencies are plotted in non-dimensional coordinates, the time instance $t = 0$ corresponds to coordinates (1, 1). The numbers along the curves denote the points corresponding to time instance $t = 20\,\text{s}$. At lower RH_{m0}, the curves reach lower values of LWC and of droplet concentration. In case of an initially narrow DSD the curve can be divided into three sections. The first section corresponds to high RH_{m0} ($RH_{m0} > 90\%$). Within this section, the droplet concentration does not decrease with decreasing LWC, which is in line with the conceptual scheme of homogeneous mixing (Fig. 1). This section corresponds to the straight horizontal line in Fig. 8a. At lower relative humidity, the droplet concentration begins to decrease with a decreasing LWC, in line with Fig. 8a. When the LWC reaches small values, the dependence of the normalized LWC on the normalized droplet concentration becomes close to linear. At an initially wide DSD (Fig. 13b), the dependence of

the LWC on droplet concentration is close to linear at all the values of RH_{m0}. This linear dependence means that the mean volume radius varies only slightly during droplet evaporation.

It is noteworthy that all the curves plotted for different initial values of RH_{m0} coincide. This coincidence can be explained by the fact that all the DSDs used depend on four parameters, namely, the three parameters of the initial Gamma distribution and on $Q(t)$ (Eq. 31). The parameters of Gamma distributions are identical for each panel in Fig. 13. Parameter $Q(t)$ monotonically increases with time. At different RH_{m0}, the values of $Q(t)$ reach the same values at different times. When the values of $Q(t)$ are the same, the DSDs and all the DSD moments are equal.

To sum up, at an initially narrow DSD and a comparatively large initial relative humidity $RH_{\mathrm{m0}} > 87\%$ phenomenon demonstrates properties typically attributed to homogeneous mixing, when a decrease in both the LWC and the effective radius takes place at unchanged droplet concentration (Figs. 8a, 9b, 11a, 13a). In contrast, in the case of an initially wide DSD, the evolution of the DSD and its moments is close to that typically attributed to inhomogeneous mixing, when droplet evaporation leads to a decrease in LWC and in droplet concentration, while the effective radius remains unchanged. During the changes of a wide DSD, its shape remains similar to itself (Fig. 7b), which is also considered typical of inhomogeneous mixing.

5. Discussion: Application of the concept of homogeneous mixing in numerical modeling

The procedure of mixing in any cloud model involves two steps. At the first step, the changes in microphysical values in each grid point are calculated using the turbulent flux divergences. In case mixing takes place between any two volumes represented by neighbouring grid points, the mixing volume containing both grid points never becomes homogeneous (*a fortiori*, the

529 microphysical values in these grid points do not become identical during one time step), so the
530 spatial gradients of the microphysical variables remain between neighbouring grid points. This
531 step represents inhomogeneous mixing at resolving scales. Mixing algorithm in models does not
532 operate with "final" equilibrium values, as assumed in the classical mixing concepts, but rather
533 with current time-dependent values. In contrast, the changes in the microphysical and
534 thermodynamical variables in the volumes represented by one grid points are often considered
535 uniform at each time step, and therefore, the modelled subgrid mixing is treated as
536 homogeneous. Therefore, in most numerical models mixing is inhomogeneous at resolved scales,
537 but homogeneous at subgrid scales.

538 The estimations in Tab. 1 indicate that mixing is homogeneous at scales lower than ~0.5 m.
539 This means that to simulate homogeneous mixing explicitly, the grid spacing should be less than
540 0.5 m. If such grid spacing is used, the separation between mixing types could be described
541 explicitly. However, grid spacing in most models significantly exceeds this value. This fact
542 brings up two questions: "What error is introduced when the spatial scale separating mixing
543 types in models is much larger than 0.5 m?" and "Why are spectral microphysics models with a
544 resolution of 40-50 m able to reproduce observed DSD and their moments with high accuracy
545 (Benmoshe et al., 2012; Khain et al., 2013, 2015; Magaritz-Ronen et al., 2014)?"

546 There are several factors that compensate errors in segregating mixing types in cloud models
547 and allow using grid scale $L > L_{pr}$ with little effect on DSD. The first factor is that mixing leads
548 to formation of cloud zones characterized by a spatial correlation scale (radius of correlation) of
549 temperature, humidity and droplet concentration of about 150-250 m (Magaritz-Ronen et al.,
550 2014). Numerical experiments with Lagrangian-Eulerian model of Sc (Magaritz-Ronen et al.,
551 2014) have shown that the results are not sensitive to the choice of parcel size, if this size is
552 substantially smaller than the spatial radius of correlation. Therefore, the mixing type has a
553 minor effect on the results of mixing at scales lower than the radius of correlation.

554 The second factor is that in-cloud mixing often takes place at conditions close to saturation.
555 At such high humidity, homogeneous and inhomogeneous mixing yield practically the same
556 results. The similarity of results for the two mixing types is due to the fact that mixing in clouds
557 is not accompanied by an appreciable phase transition.

558 The third factor was pointed out by Hill et al. (2009), who explained that stratocumulus cloud
559 evolution is insensitive to the type of sub-grid mixing since the rates of condensation/evaporation
560 caused by the resolved dynamics are by two orders of magnitude greater than the
561 condensation/evaporation rate caused by the sub-grid processes.

562 The fourth factor that permits us to treat sub-grid mixing as homogeneous near cloud
563 interfaces is that DSDs are polydisperse, which is opposite what is assumed in the conventional
564 mixing considerations. In the present study it was shown that for a broad DSD, the changes of
565 r_{eff} remain small during mixing. So, a relatively small partial evaporation of droplets provide
566 sufficient amount of water vapor for saturation of the volume. In this case homogeneous mixing
567 becomes indistinguishable from inhomogeneous. The saturation of the volume may be facilitated
568 by entrainment of water vapor from neighboring cloud volumes.
569

570 **6. Conclusions**

571

572 The present study is focused on the dynamics of DSD transformation during the evaporation
573 stage of homogeneous mixing. The results can be summarized as follows.

574 1. Analytical equations describing time evolution of normalized supersaturation and
575 normalized LWC are obtained. It is found that these time dependences are universal functions
576 of a sole non-dimensional parameter $\gamma = 1 + \frac{S_{m0}}{A_2 q_{m0}}$. In particular, the dependences of normalized
577 LWC at the final stage on the cloud air fraction, used for plotting the universal mixing diagrams,

578 are obtained analytically. These diagrams also depend on a sole non-dimensional parameter
579 $R = \frac{S_2}{A_2 q_1} < 0$, which is proportional to supersaturation in dry volume and inversely proportional
580 to liquid water mixing ratio in a cloud volume. This parameter is uniquely related with parameter
581 γ by Eq. (24). It is shown that in many cases the major changes in the LWC take place during
582 the time period of the order of the phase relaxation time τ_{pr}. The equilibrium state can be
583 reached after several τ_{pr} periods.

584 2. It is shown that the phase relaxation time is a natural time scale of mixing process. This is
585 clearly seen from the universal renormalized evaporation equations, in which the phase
586 relaxation time plays the role of a time unit. In some studies (e.g. Baker and Latham, 1979;
587 Burnet and Brenguier, 2007; Andejchuk et al., 2009) evaporation time for an individual droplet
588 under given sub-saturation is considered as a characteristic time of mixing. The present study
589 shows that only the phase relaxation time should be used as the characteristic time scale of
590 mixing since we have to consider the behavior of a large amount of droplets. Supersaturation (or
591 sub-saturation) is not a parameter that determines the phase relaxation time. Thus, the utilization
592 of the evaporation time of individual droplet (at unchanged supersaturation) as the characteristic
593 time scale of mixing is physically ungrounded. A strict relationship between the changes in
594 supersaturation and in the liquid water mixing ratio makes it impossible to consider the changes
595 in an individual droplet size and in supersaturation independently.

596 3. An important outcome of this study is demonstration of a significant difference in the
597 evaporative behavior between narrow DSD and wide DSD. It is shown that homogeneous
598 evaporation of a wide DSD is accompanied by reduction in LWC and in droplet concentration
599 due to total evaporation of small droplets. Such changes of LWC and droplet concentration are
600 qualitatively different from those in the classic concept of homogeneous mixing. As a result,
601 homogeneous mixing may be erroneously interpreted as inhomogeneous one.

4. It is shown that the evolution of DSDs and their moments in case of polydisperse DSDs, can qualitatively differ from that predicted by homogeneous mixing concept. Evaporation of a comparatively wide DSD may even lead to an increase in the effective radii and DSD high moments. This feature is typically attributed to inhomogeneous mixing.

Note that the role of DSD polydispersity in the mixing process is different from that in diffusion droplet growth in ascending parcels. In an ascending adiabatic parcel the supersaturation tends to zero with height, and the DSD width decreases with height as well. In this case, it is possible to reproduce the height dependencies and the time dependencies of supersaturation and of LWC using an "equivalent" monodisperse DSD with the same droplet concentration as a polydisperse DSDs (Pinsky et al., 2014). As regards to mixing with a polydisperse DSD, it cannot be reproduced using a monodisperse DSD, with a possible exception in case of an initially extremely narrow DSD.

Acknowledgements. This research was supported by the Israel Science Foundation (grant 1393/14), the Office of Science (BER), the US Department of Energy Award DE-SC0006788 and the Binational US-Israel Science foundation (grant 2010446). Dr. Korolev's participation was supported by Environment Canada.

Appendix A: List of Symbols

Table A1 here

626 **Appendix B. Derivation of closed equations for supersaturation and for liquid water**
627 **mixing ratio in the monodisperse DSD case.**

628

629 Let us consider motionless well-mixed adiabatic air volume having an initial supersaturation
630 $S_{m0} < 0$ and an initial liquid water mixing ratio q_{m0}.

631 1. Substitution of the formula of the liquid water mixing ratio $q = \frac{4\pi\rho_w}{3\rho_a} N r^3$ into the
632 equation for droplet radius evolution

633 $$r\frac{dr}{dt} = \frac{S}{F} \tag{B1}$$

634 leads to the equation for the decrease of q with the time

635 $$\frac{dq}{dt} = \frac{3}{F}\left(\frac{4\pi\rho_w}{3\rho_a}\right)^{2/3} N^{2/3} S q^{1/3} = B N^{2/3} S q^{1/3} \tag{B2}$$

636 where

637 $$B = \frac{3}{F}\left(\frac{4\pi\rho_w}{3\rho_a}\right)^{2/3} = const \tag{B3}$$

638 2. Equation for supersaturation is written as (Korolev and Mazin, 2003)

639 $$\frac{1}{S+1}\frac{dS}{dt} = -A_2\frac{dq}{dt} \tag{B4}$$

640 Integration of this equation under the assumption that $A_2 = const$ leads to the equation

641 $$\ln\left[S(t)+1\right] = -A_2 q(t) + C \tag{B5}$$

642 where C is determined by initial conditions at $t = 0$

643 $$C = \ln(S_{m0}+1) + A_2 q_{m0} \tag{B6}$$

644 Using Eqs. (B5) and (B6) one obtains the equation with respect to $S(t)$

645 $$S(t) = (S_{m0}+1)\exp\left\{-A_2\left[q(t) - q_{m0}\right]\right\} - 1 \tag{B7}$$

646 3. Mutual substitution of Eqs. (B2) and (B7) leads to the closed differential equations for

647 $q(t)$ and $S(t)$

648 $$\frac{dq}{dt} = BN^{2/3}\left[(S_{m0}+1)\exp\{-A_2(q-q_{m0})\}-1\right]q^{1/3} \quad \text{(B8)}$$

649 $$\frac{1}{S+1}\frac{dS}{dt} = -A_2BN^{2/3}S\left(q_{m0} - \frac{1}{A_2}\ln\frac{S+1}{S_{m0}+1}\right)^{1/3} \quad \text{(B9)}$$

650 Eqs. (B8) and (B9) should be solved with initial conditions $q(0) = q_{m0}$ and $S(0) = S_{m0}$

651 respectively.

652 4. In case $|S_{m0}| << 1$, supersaturation is close to zero all the time $|S(t)| << 1$ and Eqs. (B7-B9)

653 can be simplified as follows

654 $$S(t) = S_{m0} - A_2\left[q(t) - q_{m0}\right] \quad \text{(B10)}$$

655 $$\frac{dq}{dt} = -BN^{2/3}\left(A_2q^{4/3} - (A_2q_{m0} + S_{m0})q^{1/3}\right) \quad \text{(B11)}$$

656 $$\frac{dS}{dt} = -B(A_2N)^{2/3}(A_2q_{m0} + S_{m0} - S)^{1/3}S \quad \text{(B12)}$$

657

658 5. Then one can obtain Eqs. (B10-B12) in a non-dimensional form. Let us define time scale

659 $\tau_{m0} = \left(BA_2N^{2/3}q_{m0}^{1/3}\right)^{-1}$, normalized liquid water mixing ratio $\tilde{q} = \frac{q}{q_{m0}}$, normalized supersaturation

660 $\tilde{S} = \frac{S}{A_2q_{m0}}$, and non-dimensional time $\tilde{t} = t/\tau_{m0} = BA_2N^{2/3}q_{m0}^{1/3}t$. The Eqs. (B10-B12) can be

661 rewritten in a non-dimensional form as

662 $$\tilde{S}(\tilde{t}) = -\tilde{q}(\tilde{t}) + \gamma \quad \text{(B13)}$$

663 $$\frac{d\tilde{q}}{d\tilde{t}} = \tilde{q}^{1/3}\left(\gamma - \tilde{q}\right) \quad \text{(B14)}$$

664 $$\frac{d\tilde{S}}{d\tilde{t}} = -(\gamma - \tilde{S})^{1/3}\tilde{S} \quad \text{(B15)}$$

where non-dimensional parameter $\gamma = 1 + \frac{S_{m0}}{A_2 q_{m0}}$ depends on initial supersaturation S_{m0} and initial liquid water mixing ratio q_{m0}. Eq. (B14) should be solved with initial condition $\tilde{q}(0) = 1$ and Eq. (B15) should be solved with initial condition $\tilde{S}(0) = \frac{S_{m0}}{A_2 q_{m0}} < 0$. Note that Eqs. (B14) and (B15) are rigidly connected by Eq. (B13).

References

Andejchuk, M., Grabowski, W. W., Malinowski, S. P., and Smolarkiewicz, P. K.: Numerical simulation of cloud–clear air interfacial mixing: homogeneous vs. inhomogeneous mixing., *J. Atmos. Sci.*, **66**, 2493–2500, 2009.

Anthes, R.A.,: Tropical cyclones-Their evolution, structure, and effects. Monograph 41, Amer. Meteorol. Soc., 208 pp, 1982

Baker, M., and J. Latham: The evolution of droplet spectra and the rate of production of embyonic raindrops in small cumulus clouds. *J. Atmos. Sci.*, **36,** 1612–1615, 1979.

Baker, M., R. G. Corbin, and J. Latham: The influence of entrainment on the evolution of cloud drop spectra: I. A model of inhomogeneous mixing. *Quart. J. Roy. Meteor. Soc.*, **106,** 581–598, 1980.

Baker M. B. and J. Latham: A diffusive model of the turbulent mixing of dry and cloudy air. *Quart. J. R. Met.* Soc., **108**, 871-898, 1982

Bar-Or R. Z., I. Koren, O. Altaratz and E. Fredj: Radiative properties of humidified aerosol in cloudy environment. *Atmos. Res.*, **118**, 280–294, 2012.

Benmoshe, N., M. Pinsky, A. Pokrovsky, and A. Khain: Turbulent effects on the microphysics and initiation of warm rain in deep convective clouds: 2-D simulations by a spectral mixed-phase microphysics cloud model. *J. Geophys. Res.*, **117**, 1–20, 2012.

688 Benmoshe N., M. Pinsky, A. Pokrovsky and A. Khain: Turbulent effects on microstructure
689 and precipitation of deep convective clouds as seen from simulations with a 2-D spectral
690 microphysics cloud model. *J. Geop. Res*., **117**, D06220, 2012.
691 Blyth, A. M., Choularton, T. W., Fullarton, G., Latham, J., Mill, C. S., Smith, M. H., and
692 Stromberg, I. M.: The Influence of entrainment on the evolution of cloud droplet spectra. 2. Field
693 experiments 5 at Great Dun Fell, *Q. J. Roy. Meteor. Soc*., **106**, 821–840, 1980.
694 Burnet, F., and J-L. Brenguier: Observational study of the entrainment-mixing process in
695 warm convective clouds. *J. Atmos. Sci.*, **64,** 1995–2011, 2007.
696 Denvich B. J., P. Bartello, J-L. Brenguier, L.R. Collins, W.W. Grabowski, R.H.A. Ijzermans,
697 S.P. Malinovski, M.W. Reeks, J.C. Vassilicos, L-P. Wang, and Z. Warhaft: Droplet growth in
698 warm turbulent clouds. *Q. J. Roy. Meteorol. Soc.,* **138**, 1401-1429, 2012.
699 Dimotakis P. E.: Turbulent mixing, *Annu. Rev. Fluid Mech*., **37**, 329-356, 2005.
700 Ferrier, B.S. and R.A. Houze: One-dimensional time dependent modeling of GATE
701 cumulonimbus convection. *J. Atmos. Sci.,* **46**, 330-352, 1989.
702 Gerber H, Frick G, Jensen J.B, and Hudson J.G.: Entrainment, mixing, and microphysics in
703 trade-wind cumulus. *J. Meteorol. Soc. Jpn.,* **86A**. 87-106, 2008.
704 Ghan S. J., Hayder Abdul-Razzak, A. Nenes, Yi Ming, Xiaohong Liu, M. Ovchinnikov, B.
705 Shipway, N. Meskhidze, Jun Xu and X. Shi: Droplet nucleation: Physically-based
706 parameterizations and comparative evaluation, *J. Adv. Model. Earth Syst*., 3, M10001, 33 pp.
707 DOI:10.1029/2011MS000074, 2011.
708 Goix P. J. and L. Talbot: Turbulent counter flow diffusion flame structure and dilution
709 effects combustion. *Science and Technology*, 79, #4-6, 1991.
710 Hill, A. A., G. Feingold, and H. Jiang: The influence of entrainment and mixing assumption
711 on aerosol–cloud interactions in marine stratocumulus. *J. Atmos. Sci.*, 66, 1450–1464, 2009.

712 Jeffery, C. A.: Inhomogeneous cloud evaporation, invariance, and Damköhler number. J.
713 Geophys. Res. 112, D24S21, doi:10.1029/2007JD008789
714 Kerstein A. R.: Linear eddy modelling of turbulent scalar transport and mixing, *Comb. Sci.*
715 *Technol*., 60, 391-421, 1988.
716 Kerstein A. R.: Linear-eddy modelling of turbulent transport. Part 6. Microstructure of
717 diffusive scalar mixing fields. *J. Fluid Mech*., **231**, 361-394, 1991.
718 Khain A., Thara V. Prabha, Nir Benmoshe, G. Pandithurai, M. Ovchinnikov: The mechanism
719 of first raindrops formation in deep convective clouds. *J. Geophys. Res.* Atmospheres**. 118**,
720 9123–9140, 2013.
721 Khain A.P. , K. D. Beheng, A. Heymsfield, A. Korolev, S.O. Krichak, Z. Levin, M. Pinsky,
722 V. Phillips, T. Prabhakaran, A. Teller, S.C. van den Heever, J.-I. Yano: Representation of
723 microphysical processes in cloud-resolving models: spectral (bin) microphysics vs. bulk
724 parameterization. *Review of Geophysics* (in press) , 2015
725 Knight C. A. and L. J. Miller: Early radar echoes from small, warm cumulus: Bragg and
726 hydrometeor scattering. *J. Atmos. Sci.*, **55**, 2974-2992, 1998.
727 Korn G. A. and T. M. Korn: Mathematical handbook for scientists and
728 engineers: Definitions, theorems, and formulas for reference and review. Courier Corporation –
729 Mathematics - 1130 pp, 2000.
730 Korolev, A.V.: The influence of suresaturation fluctuations on droplet size spectra formation.
731 *J. Atmos. Sci.*, **52**, 3620-3634, 1995.
732 Korolev, A. V., and G. A. Isaac: Drop growth due to high supersaturation caused by isobaric
733 mixing. *J. Atmos. Sci.*, **57,** 1675–1685, 2000.
734 Korolev A., V, Isaac, G. A.: Phase transformation of mixed-phase clouds. *Q. J. Roy.*
735 *Meteorol. Soc*. **129**, 19-38, 2003.

736 Korolev, A. V., and I. P. Mazin: Supersaturation of water vapor in clouds. *J. Atmos. Sci.,* **60,**
737 2957–2974, 2003.
738 Korolev A., A. Khain, M. Pinsky, and J. French: Theoretical investigation of mixing in warm
739 clouds. Part 1: Classical concept. Submitted, 2015
740 Kumar B, J. Schumacher, and R. A. Shaw: Cloud microphysical effects of turbulent mixing
741 and entrainment. *Theor. Comput. Fluid Dyn.*, **27**, 361–376, 2013.
742 Latham, J. and Reed, R. L.: Laboratory studies of effects of mixing on evolution of cloud
743 droplet spectra, *Q. J. Roy. Meteor. Soc*., **103**, 297–306, 1977.
744 Lehmann, K., H. Siebert, R. A. Shaw: Homogeneous and inhomogeneous mixing in cumulus
745 clouds: Dependence on local turbulence structure. *J. Atmos. Sci.*, **66**, 3641–3659, 2009.
746 Mazin, I. P.: Effect of phase transition on formation of temperature and humidity
747 stratification in clouds. *Proc. Int. Conf. on Cloud Physics.* Toronto, Ontario, Canada, Amer.
748 Meteor. Soc., 132– 137, 1968.
749 Magaritz-Ronen L., M. Pinsky, and A. Khain: Effects of turbulent mixing on the structure
750 and macroscopic properties of stratocumulus clouds demonstrated by a Lagrangian trajectory
751 model. *J. Atmos. Sci.,* **71**, 1843–1862, 2014.
752 Monin, A.S. and Yaglom, A.M.: "Statistical Fluid Mechanics: Mechanics of Turbulence",
753 vol. **2**, MIT Press. 911 pp., 1975.
754 Pinsky, M. and A. P. Khain: Effects of in-cloud nucleation and turbulence on droplet
755 spectrum formation in cumulus clouds. *Quart. J. Roy. Meteorol. Soc*., **128**, 1–33, 2002.
756 Pinsky M., I.P. Mazin, A. Korolev, and A. Khain: Supersaturation and diffusional drop
757 growth in liquid clouds, *J. Atmos. Sci.*, **70**, 2778-2793, 2013.
758 Pinsky M., I. P. Mazin, A. Korolev and A. Khain: Supersaturation and diffusional droplet
759 growth in liquid clouds: Polydisperse spectra. *J. Geophys. Res., Atmospheres,* **119**, 12,872–
760 12,887, 2014

761 Pruppacher, H.R., Klett, J.D.: Microphysics of clouds and precipitation. 2nd edn. Oxford
762 Press, 914 p. , 1997

763 De Rooy, W. C., P. Bechtold, K. Fröhlich, C. Hohenegger, H. Jonker, D. Mironov, A. P.
764 Siebesma, J. Teixeira and J-I Yano: Entrainment and detrainment in cumulus convection: an
765 overview, *Q. J. Royal Met. Soc*., **139**, 1–19, 2013.

766 Stull, Roland B.: An Introduction to Boundary Layer Meteorology. Springer, Netherlands,
767 666 pp, 1988.

768 Troen, I. and L. Mahrt: A simple model of the atmospheric boundary layer: Sensitivity to
769 surface evaporation. *Boundary Layer Met.* **37**, 129-148, 1986.

770 Warhaft Z.: Passive scalars in turbulent flows. *Annu. Rev. Fluid Mech*., **32**, 203–240, 2000.

771 Warner J.: The microstructure of cumulus cloud. Part 1: general features of the droplet
772 spectrum, *J. Atmos. Sci.*, **26**, 1049-1059, 1969.

773

774

775

776 **Table 1.** Linear scales of volumes experiencing homogeneous mixing at conditions typical of
777 different cloud types.

Cloud type	N, cm^{-3}	LWC gm^{-3}	r, μm	Dissipation rate, cm^2/s^3	Phase relaxation time, s	Phase scale, m
Maritime Convective	100	2.0	16.8	300	2.01	0.49
Maritime Stratocumulus	100	0.5	10.6	10	3.19	0.18
Weak Stratocumulus	100	0.2	7.8	5	4.33	0.2
Continental Convective	500	2	8.0	500	0.75	0.6

778

779

780

781 **Table 2** Estimations of mixing results at different environmental conditions*

T (^{o}C)	A_2	q_1, g/kg	RH_2 %	μ (cloud fraction)	$R\frac{1-\mu}{\mu}$	Result of mixing
$T = 0^oC$	400	1.0	95	0.5	-0.125	cloudy
$T = 0^oC$	400	1.0	50	0.5	-1.25	Non-cloudy
-10^oC	700	2.0	95	0.5	-0.036	cloudy
-10^oC	700	2.0	50	0.5	-0.36	cloudy
-20^oC	1500	2.0	95	0.5	-0.017	cloudy
-20^oC	1500	2.0	50	0.5	-0.17	cloudy
-20^oC	1500	2.0	95	0.1	-0.153	cloudy
-20^oC	1500	2.0	50	0.1	-1.53	Non-cloudy

782 * The values A_2 are estimated as proposed by Pinsky et al., (2013).

783

784

785 **Tab.3** Parameters of the initial Gamma distributions

DSD	N_{m0}, cm^3	α	β, μm	Modal radius, μm	LWC, g/m^3
Narrow	264.2	101.0	0.1	10.0	0.587
Wide	71.0	4.3	3.1	10.0	0.587

786

787

788

789 **Tab. A1. List of symbols**

790

Symbol	Description	Units
A_2	$\frac{1}{q_v}+\frac{L^2}{c_p R_v T^2}$, coefficient	nd
B	$\frac{3}{F}\left(\frac{4\pi\rho_w}{3\rho_a}\right)^{2/3}$, coefficient	$m^2\ s^{-1}$
C	constant of integration	nd
c_p	specific heat capacity of moist air at constant pressure	$J\ kg^{-1}K^{-1}$
$\mathscr{D}$	coefficient of water vapour diffusion in the air	$m^2\ s^{-1}$
e	water vapor pressure	$N\ m^{-2}$
e_S	saturation vapour pressure above a flat water surface	$N\ m^{-2}$
F	$F=\frac{\rho_w L^2}{k_a R_v T^2}+\frac{\rho_w R_v T}{e_S(T)\mathscr{D}}$, coefficient	$m^{-2}\ s$
$f(r,t)$	droplet size distribution	m^{-4}
$f_0(r_0)$	droplet size distribution after the first stage of mixing	m^{-4}
k_a	coefficient of air heat conductivity	$J\ m^{-1}s^{-1}K^{-1}$
L_{mix}	characteristic spatial scale of mixing	m
L_{pr}	spatial scale of phase relaxation	m
L	latent heat for liquid water	$J\ kg^{-1}$
N	droplet concentration	m^{-3}
N_1	droplet concentration in a cloud volume	m^{-3}
N_{m0}	droplet concentration after the first stage of mixing	m^{-3}
p	pressure of moist air	$N\ m^{-2}$
q	liquid water mixing ratio	kg/kg
q_1	liquid water mixing ratio in a cloudy volume	kg/kg
q_{m0}	liquid water mixing ratio after the first stage of mixing	kg/kg
q_w	liquid water content (LWC)	gm^{-3}

q_{w0}	LWC after the first stage of mixing	gm^{-3}
q_v	water vapor mixing ratio	kg/kg
$\tilde{q}$	normalised liquid water mixing ratio equal to normalized LWC	nd
$\tilde{q}_{\min}$	normalized equilibrium liquid water mixing ratio equal to normalized equilibrium LWC	nd
Q	change of square of droplet radius	m^2
r	droplet radius	m
R	$\frac{S_2}{A_2 q_1}$	nd
R_a	specific gas constant of moist air	$J\ kg^{-1}K^{-1}$
R_v	specific gas constant of water vapor	$J\ kg^{-1}K^{-1}$
S	$e/e_w - 1$, supersaruration over water	nd
S_{m0}	supersaturation after the first stage of mixing	nd
S_2	supersaturation in a dry volume	nd
$\tilde{S}_{\max}$	maximal normalized supersaturation	nd
$\tilde{S}$	normalized supersaturation	nd
T	temperature	K
T_1	temperature in a cloud volume	K
T_2	temperature in a dry volume	K
t_e	normalized evaporation time	nd
t	time	s
$\tilde{t}$	non-dimensional time	nd
$x(\tilde{t})$	non-dimensional variable	nd
α	parameter of the Gamma distribution	nd
β	parameter of the Gamma distribution	m^{-1}
χ	$\gamma^{1/3}$, non-dimensional parameter	nd
ε	turbulent dissipation rate	m^2s^{-3}
γ	$1+\frac{S_{m0}}{A_2 q_{m0}}$, non-dimensional parameter	nd

δq_m	mixing ratio of liquid water required to saturate 1 kg of the cloud (or cloudy?) volume after instant mixing	nd
μ	mass fraction of cloud air	nd
ρ_a	air density	kg m^{-3}
ρ_w	density of liquid water	kg m^{-3}
τ_{pr}	phase relaxation time	s
τ_{mix}	characteristic time of mixing	s
τ_{m0}	time scale	s

"nd" denotes non-dimensional

809

810 **Figures**

811

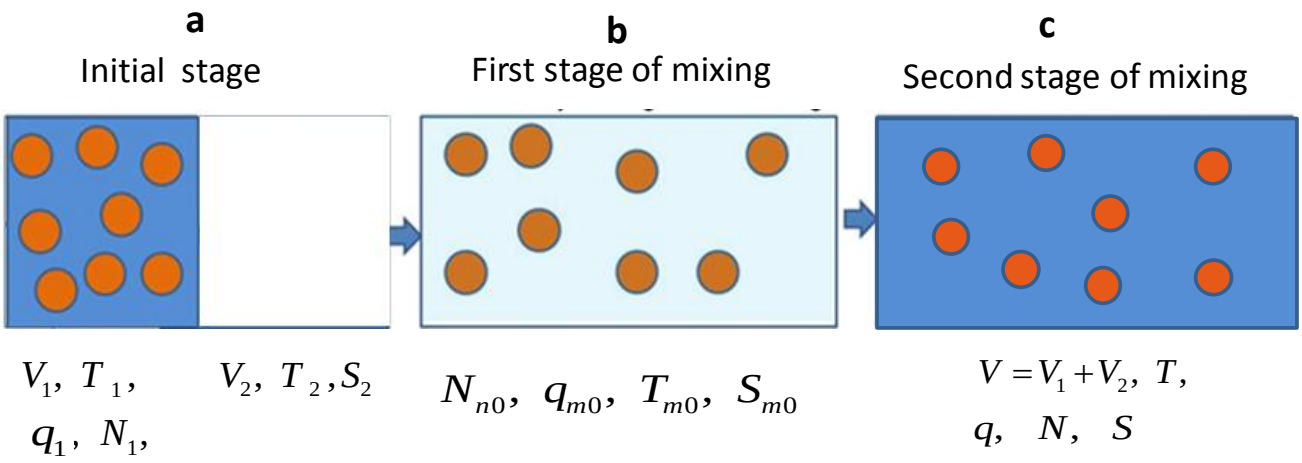

812

813

814

815 **Fig. 1**. Conceptual scheme of homogeneous mixing in case of monodisperse DSD. The
816 subsaturated volume of dry air is colored white, and the cloudy volumes with saturated air are
817 colored dark blue. The volume forming as a result of mixing after total homogenization is
818 colored light blue. Index 1 shows the initial values characterizing the initially cloudy volume.
819 Index 2 denotes initial values in the droplet-free volume. Index "$m0$" denotes values in the
820 mixing volume after the first stage of mixing.

821

822

823

824

825

826

827

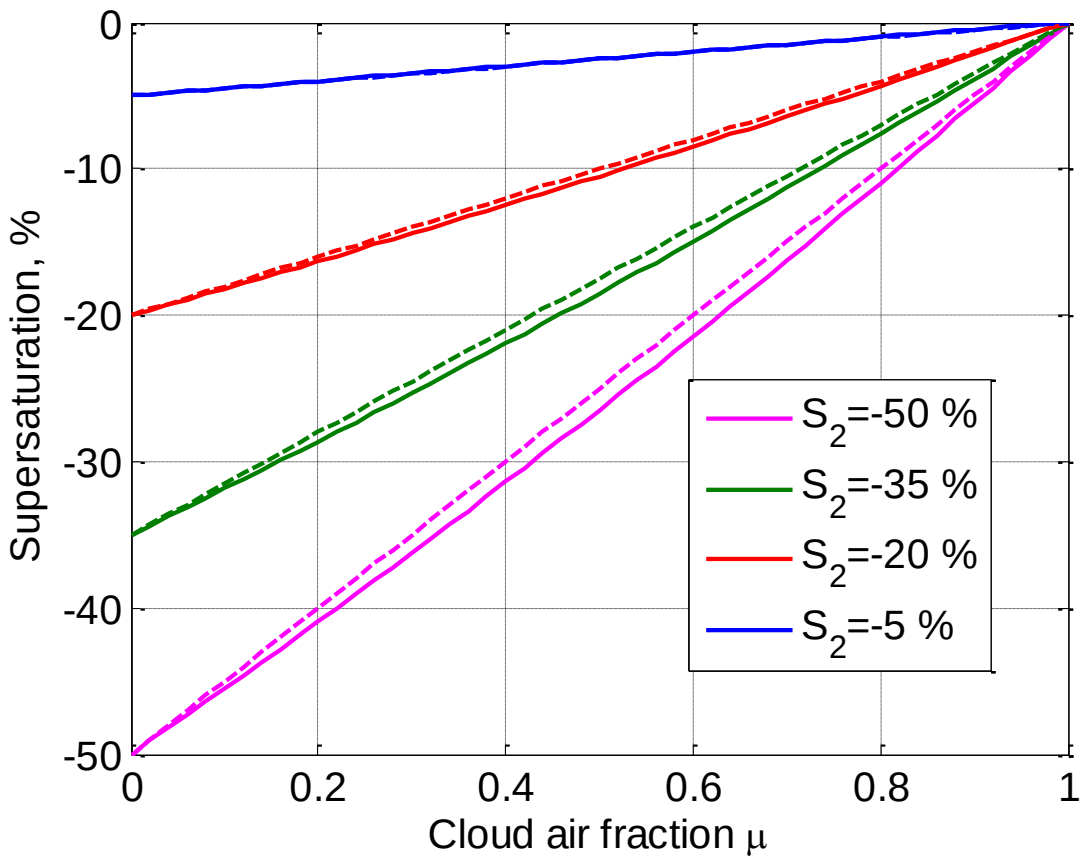

Fig. 2. Dependence of supersaturation on parameter μ: simulation results (solid line) and an approximate linear dependence calculated using Eq. (6b) (dashed line). The initial temperatures of two volumes are $T_1 = 8\,^{o}\mathrm{C}$ and $T_2 = 10\,^{o}\mathrm{C}$.

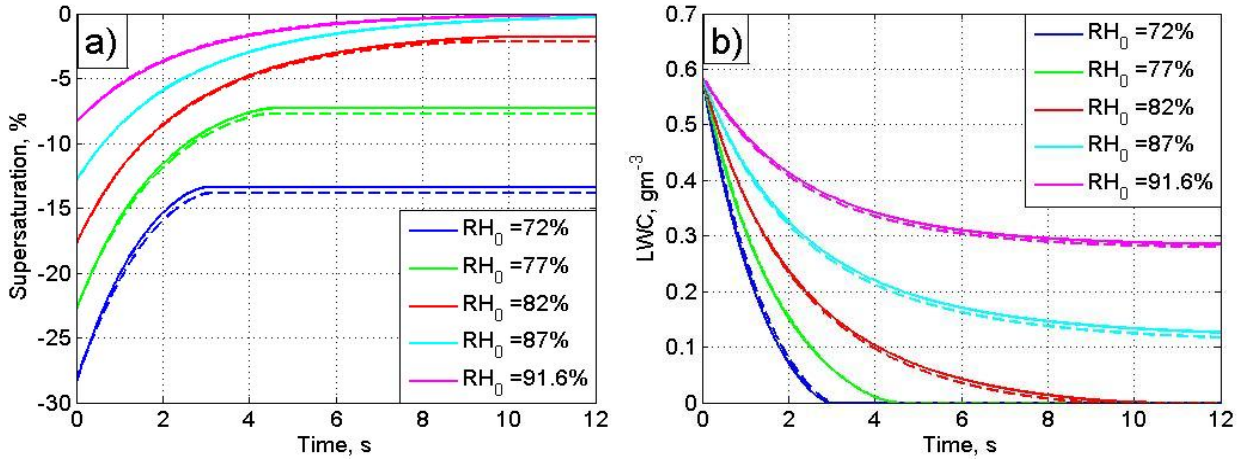

Fig. 3. Dependencies $S(t)$ (a) and $q_w(t)$ (b), calculated at different initial relative humidity RH_{m0} using closed differential equations (12,13) (solid lines) and using a parcel model (dashed lines). The calculation parameters are $T_{m0} = 10^{o}C$, $p_0 = 842$ mb, $r_0 = 10\ \mu m$, $N_{m0} = 140\ cm^{-3}$, $q_{w0} = 0.58\ gm^{-3}$.

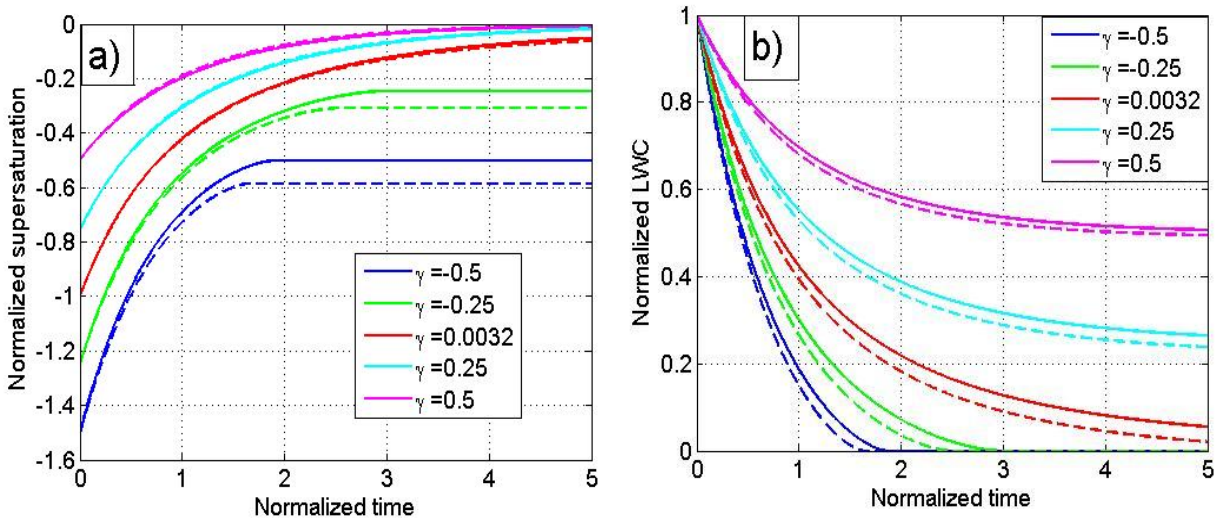

Fig. 4. Universal dependencies $\tilde{S}(\tilde{t})$ (a) and $\tilde{q}(\tilde{t})$ (b), calculated at different values of parameter γ using Eqs. (17-18) (solid lines) and using a parcel model (dashed lines).

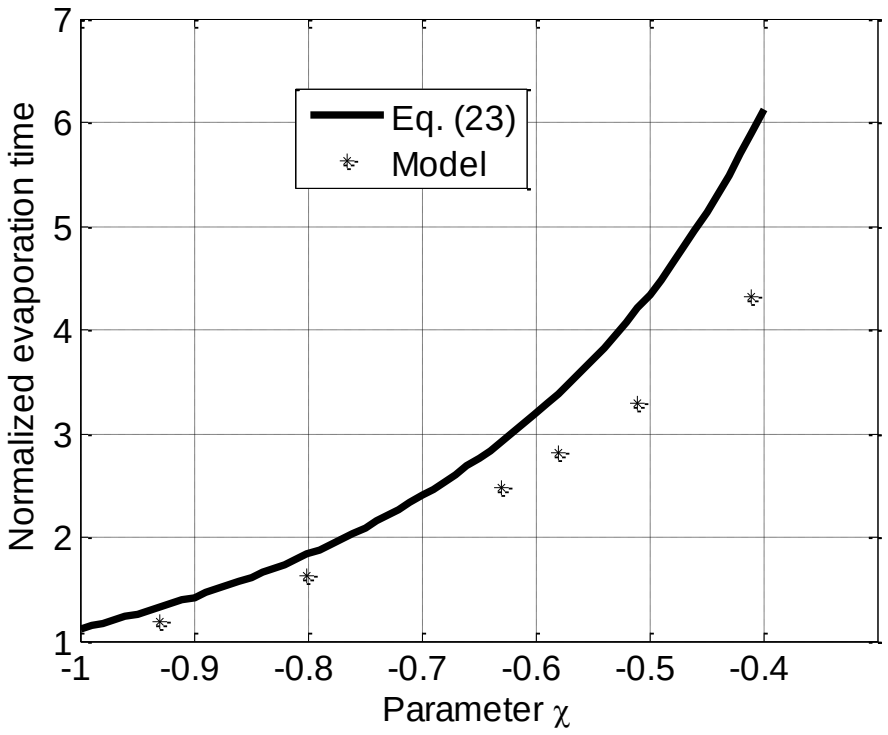

Fig. 5. Dependence of the evaporation time on parameter χ, $t_e(\chi)$. Time is measured at the relaxation time scales. The values obtained using a parcel model are shown by asterisks.

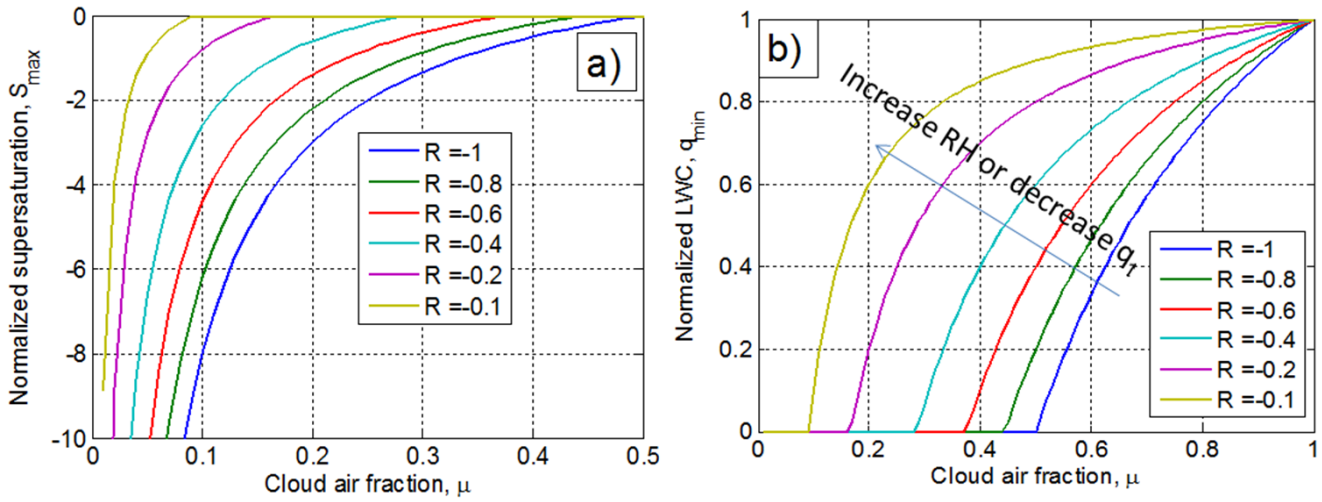

Fig. 6. Dependencies of normalized equilibrium supersaturation $\tilde{S}_{max}$ (a) and normalized equilibrium LWC (which is equal to normalized equilibrium liquid water mixing ratio) $\tilde{S}_{max}$ (b) on cloudy air fraction at the final stage of homogeneous mixing. Curves of different colors correspond to different values of non-dimensional parameter $R = \frac{S_2}{A_2 q_1}$.

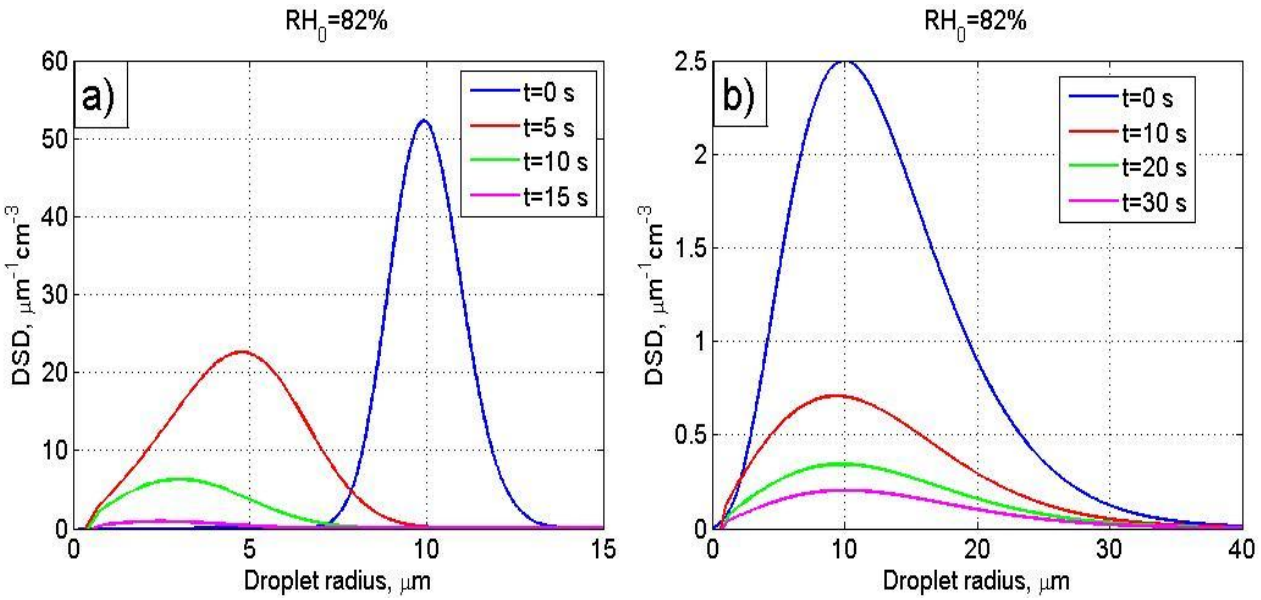

Fig. 7. Time evolution of an initially narrow DSD (a) and an initially wide DSD (b). The initial calculation parameters are the same in both examples: $T_{m0} = 10\ ^{o}C$, $p = 829$ mb, $RH_{m0} = 82\ \%$ and $q_{w0} = 0.587$ g/m^3. The parameters of the initial Gamma distributions are given in Tab. 3.

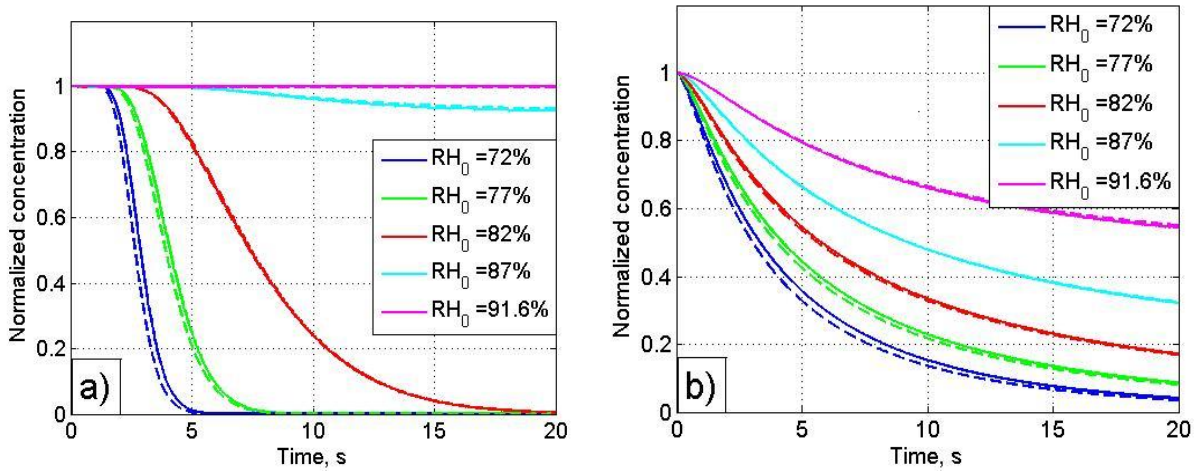

Fig.8. Time dependencies of normalized droplet concentration for an initially narrow DSD (a) and an initially wide DSD (b) at initially different values of RH_{m0} in the resulting volume. The dependencies are calculated directly using a parcel model (solid lines) and using Eq. (33) (dashed lines). The thermodynamic parameters are the same as in Fig.7. Parameters of the initial DSDs are given in Tab. 3.

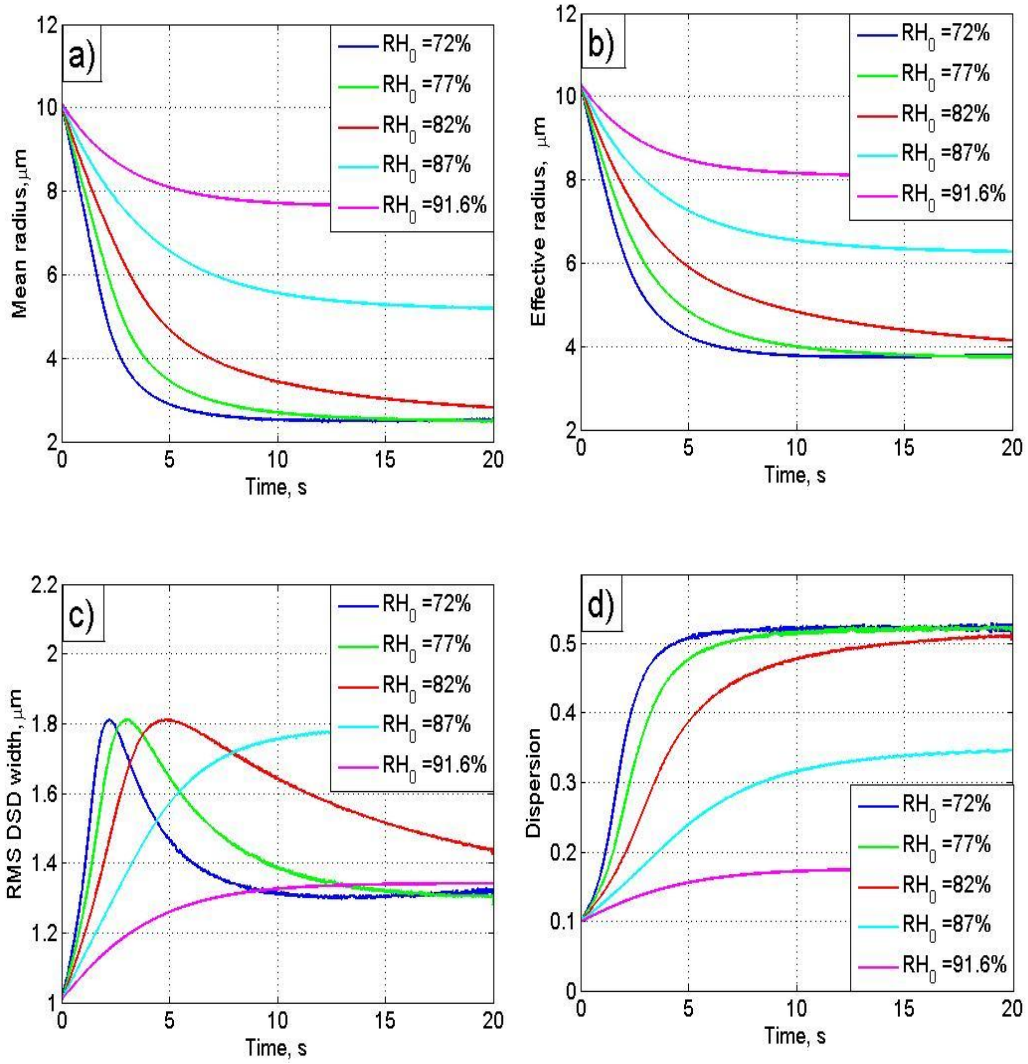

Fig. 9. Dependencies of moment functions typically used for characterizing DSD shape at different values of the initial relative humidity RH_{m0} in the resulting volume. The dependencies are calculated using a parcel model for an initially narrow DSD (Tab. 3). The thermodynamic parameters are the same as in Fig. 7.

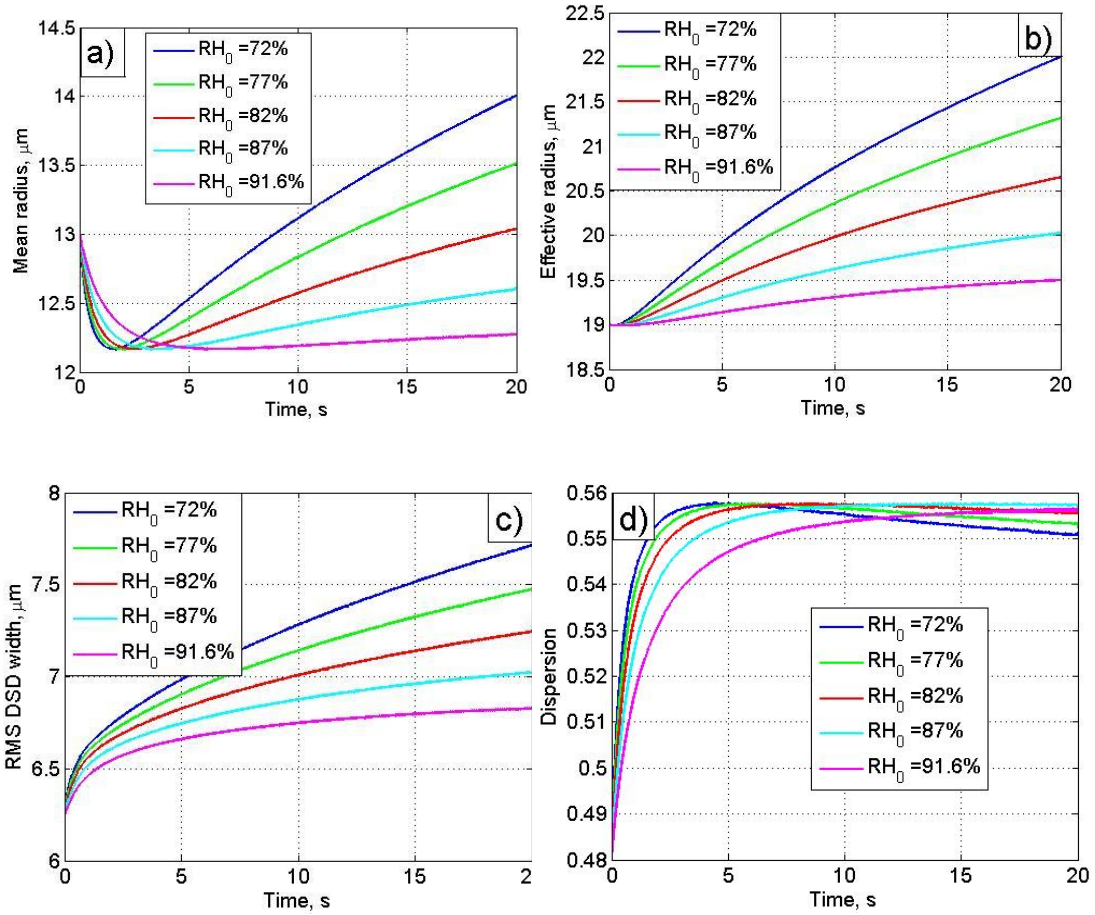

Fig. 10. The same as in Fig. 9 but for an initially wide DSD.

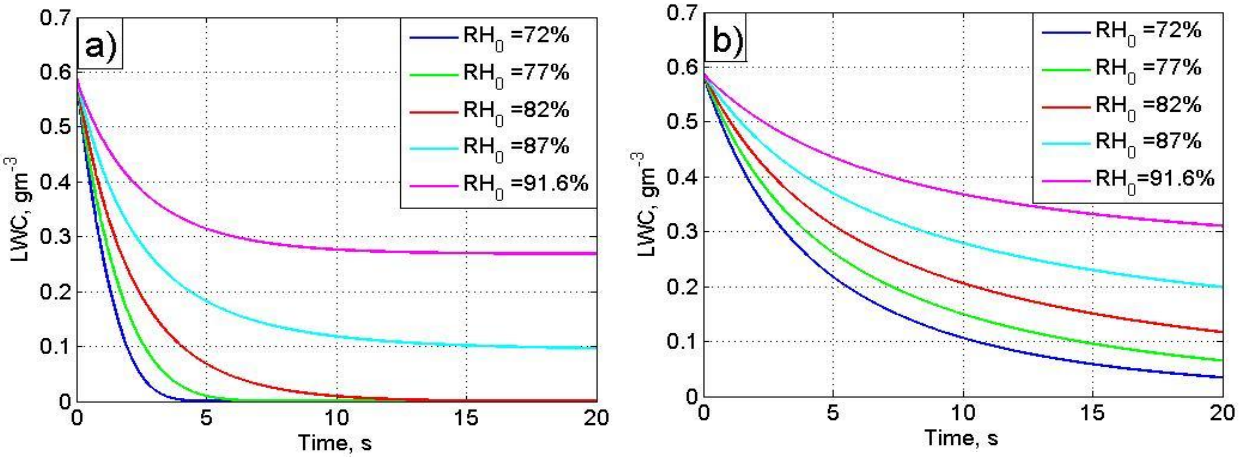

Fig. 11. Time dependencies of LWC calculated using a parcel model at different values of RH_{m0} in the resulting volume, for an initially narrow DSD (a) and an initially wide DSD (b). The thermodynamic parameters are the same as in Fig.7. The parameters of the initial DSDs are given in Tab. 3.

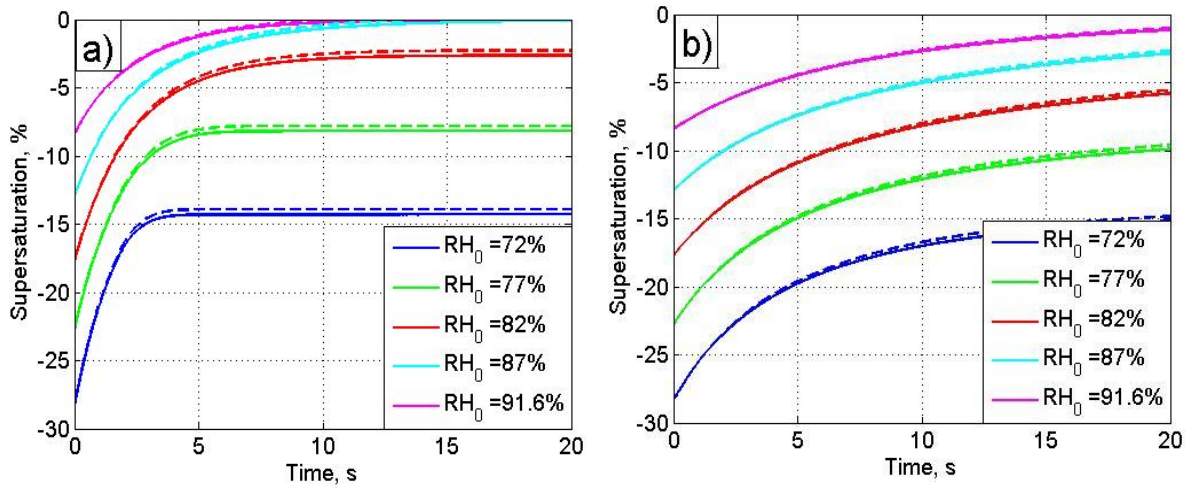

Fig. 12. Time dependencies of supersaturation calculated at different values of the initial relative humidity RH_{m0} in the resulting volume, using Eq. (8) (solid lines) and Eq. (40) (dashed lines), for an initially narrow DSD (a) and an initially wide DSD (b). The thermodynamic parameters are the same as in Fig.7. The parameters of the initial DSDs are given in Tab.3.

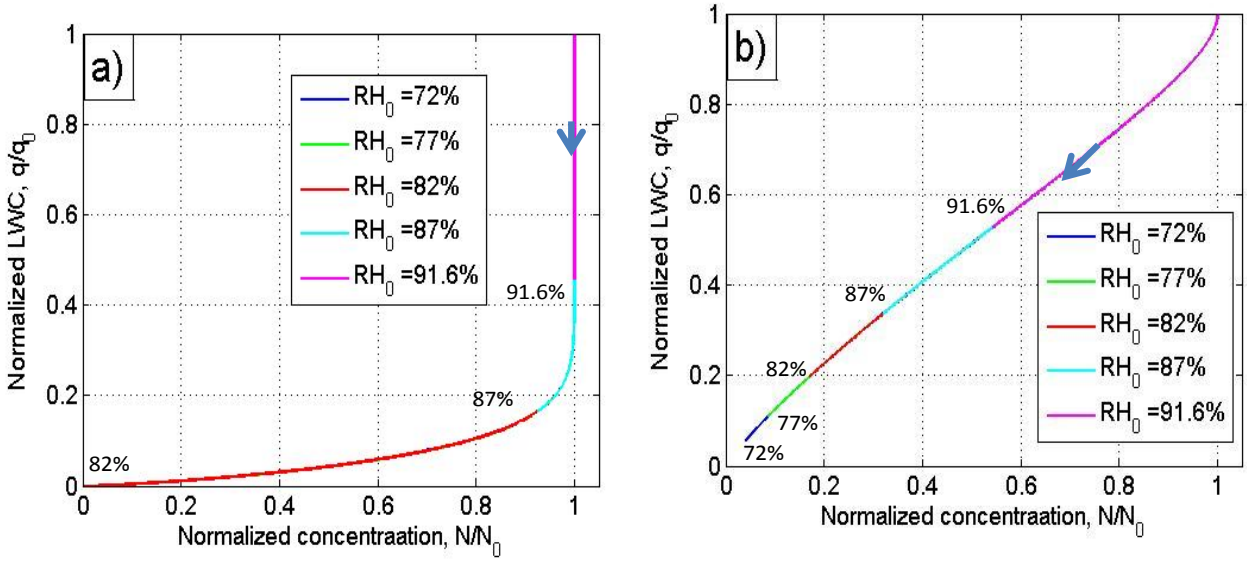

Fig. 13. Dependencies of normalized LWC on the normalized number concentration of droplets calculated at different values of the initial relative humidity RH_{m0} in the resulting volume, for an initially narrow DSD (a) and an initially wide DSD (b). The thermodynamic parameters are the same as in Fig.7. The parameters of the initial DSDs are given in Tab. 3. Arrows denote the direction of increasing time.